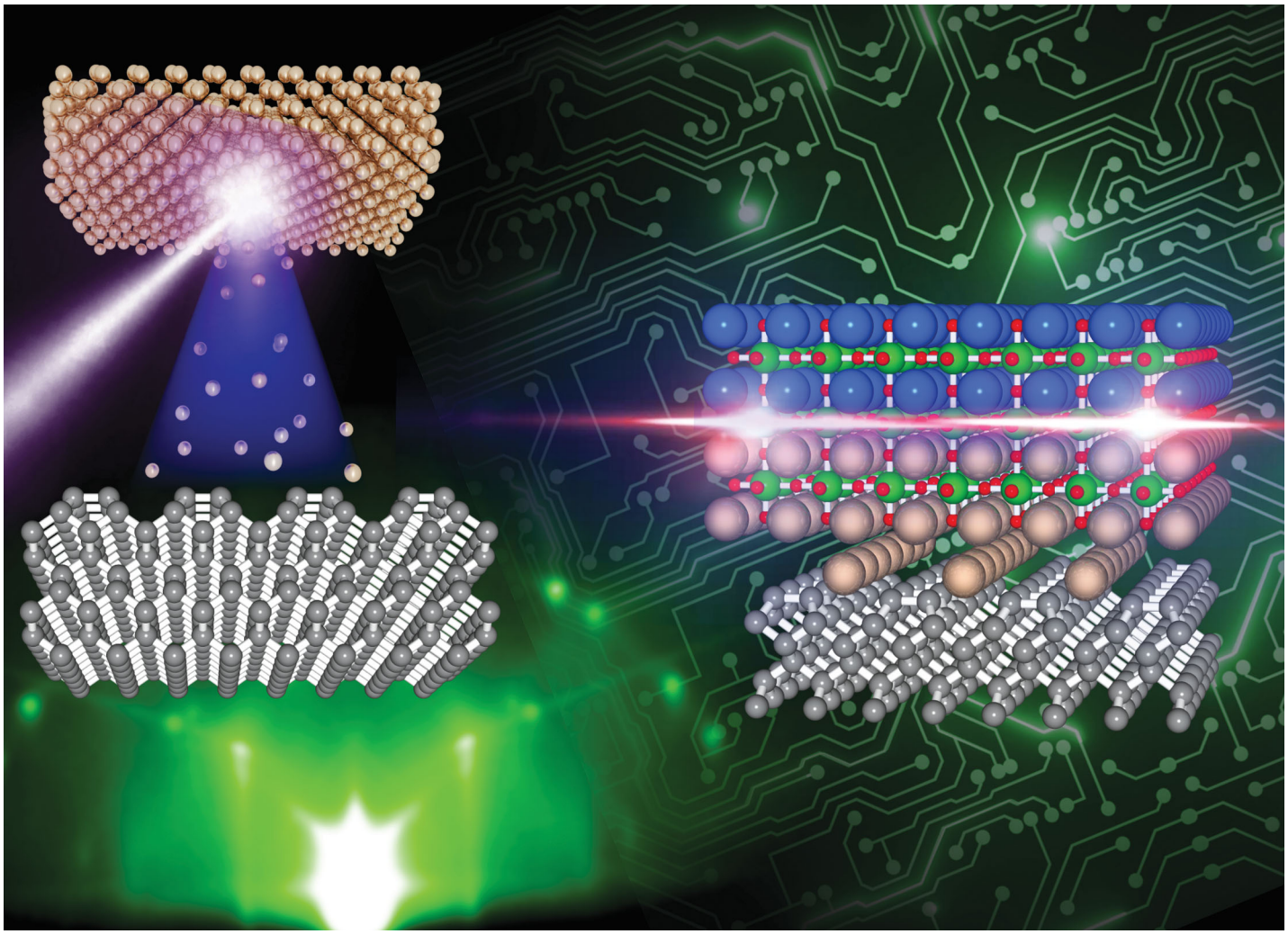

Showcasing research from the Jožef Stefan Institute, Slovenia, University of Antwerp, Belgium, and University of Twente, The Netherlands.

Growth mechanism of epitaxial $SrTiO_3$ on a (1×2) + (2×1) reconstructed Sr(1/2 ML)/Si(001) surface

A mechanism for epitaxial integration of $SrTiO_3$ with (1×2) + (2×1) reconstructed Sr(1/2 ML)/Si(001) surface using an all-pulsed laser deposition technology was determined. The results of the study represent a milestone for exploitation of the rich electrical, magnetic and optical properties of various oxides for next generation electronics.

As featured in:

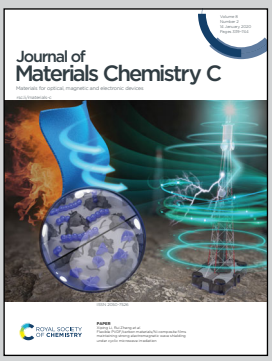

See Matjaž Spreitzer *et al.*, *J. Mater. Chem. C*, 2020, **8**, 518.

ROYAL SOCIETY OF CHEMISTRY

rsc.li/materials-c

Registered charity number: 207890

Journal of Materials Chemistry C

PAPER

View Article Online
View Journal | View Issue

Cite this: J. Mater. Chem. C, 2020, 8, 518

Growth mechanism of epitaxial $SrTiO_3$ on a (1 × 2) + (2 × 1) reconstructed Sr(1/2 ML)/Si(001) surface†

Matjaž Spreitzer, ‡*[a] Dejan Klement,‡§[a] Ricardo Egoavil,[b] Jo Verbeeck,[b] Janez Kovač,[c] Anže Založnik,[d] Gertjan Koster,[ae] Gustaaf Van Tendeloo,[b] Danilo Suvorov[a] and Guus Rijnders[e]

Received 26th July 2019,
Accepted 21st October 2019

DOI: 10.1039/c9tc04092g

rsc.li/materials-c

Sub-monolayer control over the growth at silicon–oxide interfaces is a prerequisite for epitaxial integration of complex oxides with the Si platform, enriching it with a variety of functionalities. However, the control over this integration is hindered by the intense reaction of the constituents. The most suitable buffer material for Si passivation is metallic strontium. When it is overgrown with a layer of $SrTiO_3$ (STO) it can serve as a pseudo-substrate for the integration with functional oxides. In our study we determined a mechanism for epitaxial integration of STO with a (1 × 2) + (2 × 1) reconstructed Sr(1/2 ML)/Si(001) surface using all-pulsed laser deposition (PLD) technology. A detailed analysis of the initial deposition parameters was performed, which enabled us to develop a complete protocol for integration, taking into account the peculiarities of the PLD growth, STO critical thickness, and process thermal budget, in order to kinetically trap the reaction between STO and Si and thus to minimize the thickness of the interface layer. The as-prepared oxide layer exhibits STO(001)‖Si(001) out-of-plane and STO[110]‖Si[100] in-plane orientation and together with recent advances in large-scale PLD tools these results represent a new technological solution for the implementation of oxide electronics on demand.

Introduction

Epitaxial integration of transition metal oxides with semiconductors offers various phenomena for novel device applications, specifically bringing ferroelectric, ferromagnetic, electro-optic, photocatalytic, multiferroic, piezoelectric and other properties to the well-established silicon platform.[1–4] A convenient way of integrating functional oxides on a Si(001) substrate is through a $SrTiO_3$ (STO) intermediate layer, which can be fabricated on Si(001) in epitaxial form and with high crystallinity using mainly the molecular beam epitaxy (MBE) method.[5,6] However, the run-to-run stability of the MBE deposition process and difficult stoichiometry control make this an inappropriate tool from an industrial point of view.

In this work we focus on the possibilities of using the pulsed laser deposition (PLD) technique for the synthesis of an epitaxial STO layer on Si(001) as an alternative manufacturing route compared to MBE. Deposition performed by PLD is much faster and offers stable, stoichiometric transfer, which is more easily controllable, wherein the quality of the PLD thin films can be comparable to layers synthesized by MBE.[7] Recently large-area PLD systems have become available on the market, which indicate the industrial potential of PLD.

Two main MBE strategies for fabricating epitaxial STO thin films on Si are commonly applied. The first strategy is based on the deposition of 2–4 STO MLs on Sr(1/2 ML)/Si(001) at a relatively low O_2 partial pressure in the upper 10^{-8} mbar range and a moderate temperature of 360 °C. Then the O_2 partial pressure is ramped up to the 10^{-6} mbar range for the rest of the growth.[8–11] Kinetically controlled sequential deposition (KCSD) is another approach where the deposition step is conducted at low temperature and relatively high O_2 partial pressure, followed by a high temperature and low O_2 partial pressure step.[2,12–14] The two-step procedure is repeated until the desired thickness is obtained. In some investigations the first step of

[a] Advanced Materials Department, Jožef Stefan Institute, Jamova 39, 1000 Ljubljana, Slovenia. E-mail: matjaz.spreitzer@ijs.si
[b] Electron Microscopy for Materials Science, University of Antwerp, Groenenborgerlaan 171, 2020 Antwerp, Belgium
[c] Department of Surface Engineering and Optoelectronics, Jožef Stefan Institute, Jamova 39, 1000 Ljubljana, Slovenia
[d] Department for Low and Medium Energy Physics, Jožef Stefan Institute, Jamova 39, 1000 Ljubljana, Slovenia
[e] Faculty of Science & Technology and MESA+ Institute for Nanotechnology, University of Twente, Carré, 3243, 7500 AE Enschede, The Netherlands

† Electronic supplementary information (ESI) available. See DOI: 10.1039/c9tc04092g

‡ These authors contributed equally.

§ Present address: Krka, d. d., Novo mesto, Slovenia.

the KCSD procedure was performed by the separate deposition of SrO and TiO_2 (topotactic reaction).[15–19]

The growth of STO on silicon using PLD with the introduction of different epitaxial buffer layers, mainly TiN and yttria-stabilized zirconia (YSZ)/CeO_2, has also been intensively investigated.[20] YSZ has the advantage that it can be deposited directly on a natively oxidized Si(001) substrate because it activates the decomposition of the native SiO_2.[21] Once the amorphous SiO_2 layer is removed, YSZ grows epitaxially on Si and serves as a template for overgrowth with STO.[22,23] However, the crystal quality of the oxide layer is limited due to the high lattice mismatch of these two buffer systems with Si. Therefore the use of more delicate buffer systems, such as metallic Sr and SrO, has been initiated,[24–27] while the mechanism of epitaxial integration of the first system with the STO layer represents the focus of this study.

Our purpose was to explore the possibility of using the PLD technique for the synthesis of an epitaxial STO layer on Sr(1/2 ML)/Si(001), as an alternative manufacturing route to MBE. For the preparation of the strontium buffer layer we followed the surface structure evolution through the $(3 \times 2) + (2 \times 3)$ reconstruction, described in our previous work.[24] In the present study a systematic analysis of PLD growth of STO on Si is presented, with particular emphasis on the determination of the most critical initial deposition parameters. A complete crystallographic characterization of the STO layers is given, together with the analysis of the interface structure by means of X-ray photoelectron spectroscopy (XPS), X-ray reflectivity (XRR) and transmission electron microscopy (TEM).

Materials and methods

PLD

Silicon wafers (Si-Mat, Germany) with a diameter of 200 mm were cut into substrates of 5×5 mm, which were used for thin film deposition. The substrates were boron doped (p-type with a resistivity of 1–30 Ω cm) single side polished with a thickness of 525 μm. The termination plane of the substrates was (001). The wafers were cut with an accuracy of $\pm 0.1^\circ$ along that crystal plane. The Si(001) substrate was first ultrasonically cleaned for 10 min in acetone, in order to remove organic contaminants. Then the substrate was rinsed with ethanol and dried with a nitrogen gun. The as-prepared sample was clamped to a custom-build holder made out of tantalum, loaded into the PLD chamber and prebaked at 630 °C for 12 hours. The native oxide layer was desorbed by flashing the substrate to 1200 °C for 1.5 min. After removal of the native oxide, the substrate temperature was reduced to 700 °C and the Sr-buffer layer (1/2 ML coverage) was prepared by the deposition of elemental strontium. Samples and targets were transferred in and out of the deposition chamber through a load-lock chamber that can be pumped and vented without affecting the main chamber vacuum. Samples were heated using an infrared (IR) laser, working at a wavelength of 800–820 nm, and the temperature was measured with a pyrometer, operating in a spectral range of 1.45–1.8 μm. For the temperature calculation an emissivity of 0.85 was used during the investigation of SiO_2 layer elimination and Sr buffer layer preparation. When the deposition of the STO layer was studied, the emissivity value was changed to 0.30. In all the experiments the target–substrate distance was kept constant at 55 mm. In the experiments a custom-made PLD system (TSST, the Netherlands) and KrF excimer laser (Coherent COMPexPro 205, USA) were used. For buffer layer preparation purposes a target of elemental strontium with a purity of 99.9% (MaTecK, Germany) was used. In order to prevent exposure of the strontium target to the air, a glove-box was connected to the load-lock of the PLD chamber. As a source of STO material for thin film deposition a single-crystal STO target was used (Plasmaterials, USA). Reflection high-energy electron diffraction (RHEED) was used for *in situ* monitoring of surface structure changes and thin film growth during the deposition.

TEM

The deposited silicon–oxide structure was characterized by high-angle annular dark-field (HAADF) scanning-transmission electron microscopy (STEM) and electron energy-loss spectroscopy (EELS) (Fig. 7 and Fig. S10 and S11, ESI†) performed on a FEI Titan3 microscope operated at 300 kV. HAADF-STEM images were taken using a convergence semi-angle of the electron probe of ~21 mrad and collecting at an inner detector semi-angle of ~50.5 mrad. The spatial resolution of the experiment was estimated at ~0.8 Å. STEM-EELS experiments were performed on a GIF Quantum ERS spectrometer. The EELS convergence and collection semi-angles were set to ~13 mrad and ~97.9 mrad, respectively. The energy resolution for the EELS measurements was 1.0 eV, as determined from the full width at half maximum (FWHM) of the zero-loss peak. An energy dispersion of 0.25 eV $pixel^{-1}$ was selected to collect all the Si L_{23}, Ti L_{23} and O K signals in the same spectra. The chemical elemental maps were generated by subtracting a power-law background and integrating the corresponding core-loss excitation edge for each element. The EELS spectra were analyzed using Digital Micrograph software.

XRR

The density, thickness and roughness of the STO layers on a substrate were quantitatively determined from the reflectivity curve using the X'Pert Reflectivity software package version 1.3a. The thickness analysis was performed using two different approaches: direct and Fourier methods.

XRD

X-ray diffraction (XRD) characterization was performed with a PANalytical Empyrean diffractometer. A symmetric or 2theta/theta scan with parallel beam geometry was used for phase analysis and determination of the out-of-plane thin film orientation. A phi scan was performed for the determination of the in-plane orientation of the STO layer with respect to the Si substrate. X-ray diffraction reciprocal space maps (RSMs) were recorded in order to obtain the unit cell parameters (PANalytical B. V., The Netherlands, version 4.3a).

XPS

The types of chemical bonds formed at the STO/Si interface were obtained *ex situ* using an XPS system (Physical Electronics, Inc., USA) equipped with a monochromatic AlKα (1486.6 eV) photon source, an electrostatic hemispherical energy analyzer and a multichannel electron detection system. The take-off angle of emitted photoelectrons was 45° with respect to the sample surface. The survey spectra were taken in a range of binding energies from 0 to 1200 eV with a pass energy of 187.85 eV. The high-resolution narrow scan spectra of Si 2p, Sr 3d, Ti 2p, O 1s and C 1s were acquired with a pass energy of 23.50 eV. For the investigation of the Ti oxidation state in amorphous STO layers deposited at room temperature, depth-profile analysis was performed by sequential sputtering of the sample with an ion beam. Ion sputtering was conducted with a 3 keV Ar^+ beam rastered over a 3 × 3 mm^2 area.

RBS

The stoichiometry of the STO thin films was quantified using Rutherford backscattering spectroscopy (RBS), which was used for the optimization of the laser fluence. A beam of monoenergetic $^4He^+$ ions with an energy of 2.5 MeV was directed at a target, impacting perpendicularly to the sample surface. The energy of the ions, which are scattered backwards at a 170° angle with respect to the probing beam, was analyzed. Simulations of backscattering spectra were performed using SIMNRA software, version 6.06.

Results and discussion

Optimization of the background gas pressure

To determine the optimal deposition pressure, different samples were prepared by the deposition of 6000 pulses at different Ar pressures: in a vacuum (app. 1×10^{-8} mbar), and at 0.01, 0.02, 0.03, 0.04, 0.05, 0.1 and 0.15 mbar. The deposition of the STO material was performed at room temperature, while the repetition rate, fluence, spot size and target-to-substrate distance were kept constant at 1 Hz, 1.5 J cm^{-2}, 0.58 mm^2 and 5.5 cm, respectively.

The comparison of X-ray reflectivity (XRR) curves for samples deposited at different argon pressures is shown in Fig. 1. From the position of the critical angle, ω_c, which varies significantly with the background pressure (Fig. S1, ESI†), the density of the amorphous STO layers was determined based on fitting (Table S1, ESI†). As a reference, the reflectivity curve for the STO substrate was simulated and is shown in Fig. S1 (ESI†) as a black curve. Layers with the highest density (~84% of the theoretical value) can be prepared in the pressure range from a vacuum up to 0.03 mbar, with the value slowly decreasing from 4.34 to 4.25 g cm^{-3}, respectively. As the pressure further increases from 0.03 to 0.15 mbar the density continuously decreases, reaching 3.39 g cm^{-3} (66% of the theoretical value) for a pressure of 0.15 mbar.

The background pressure affects also the thickness of the deposited layer. The deposition rate at higher pressures is expected to be lower due to collisional scattering and broadening of the vapour plume, which results in a lower layer thickness. The thickness of the STO layers was determined by Fourier and direct methods and good agreement between the results was shown. Calculated by the Fourier method the thickness decreases from 41.9 to 31.5 nm as the background pressure increases from vacuum conditions to 0.15 mbar (Table S1, ESI†).

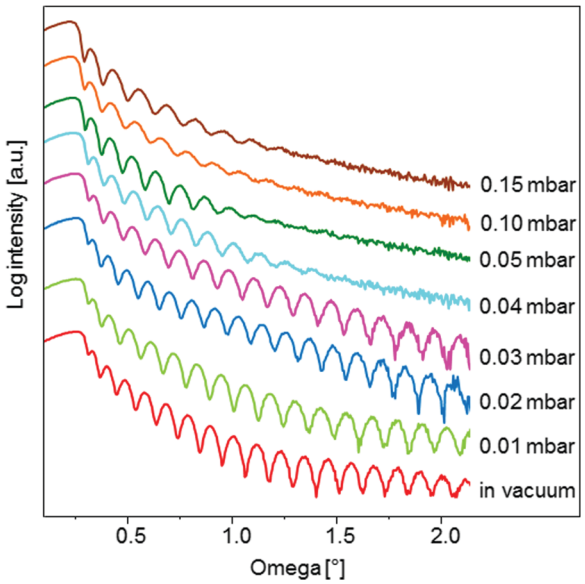

Fig. 1 Comparison of the X-ray reflectivity curves for samples prepared at different Ar background pressures.

Another very informative feature of the reflectivity curve is the damping of the fringes. The presence of oscillations at high ω angles indicates a smooth surface. This is the case for samples prepared in a vacuum, and at 0.01, 0.02 and 0.03 mbar Ar pressure (Fig. 1). For the sample deposited at 0.04 mbar the fringes vanish already at 1.45° as a result of a significantly higher surface roughness compared to the samples prepared at a lower background pressure. An important similarity between the reflectivity curves can be observed for the samples prepared at 0.05 mbar, 0.10 mbar and 0.15 mbar pressure. All three curves exhibit oscillations up to the same ω angle, indicating a constant surface roughness for layers deposited at pressure ≥0.05 mbar. This observation was additionally confirmed by atomic force microscopy (AFM) (Fig. S3, ESI†). The samples deposited at 0.05 mbar, 0.10 mbar and 0.15 mbar exhibit the same root mean square roughness (R_q) of 0.45 nm. On the other hand, a lower surface roughness was obtained for samples deposited in a vacuum (R_q = 0.31 nm) and at 0.01 mbar (R_q = 0.27 nm).

As the pressure is raised, the plume impacts the substrate at a progressively smaller velocity due to the interaction of the plasma species with the background gas. When the species reach the substrate surface, their kinetic energy is converted into surface diffusion energy, which affects the final surface roughness. Another important property of the plume is its transition towards diffusion-like propagation. This transition is related to plume stopping, which occurs at progressively shorter distances from the target surface by increasing the

background pressure. Thus, the constant surface roughness for the samples deposited at pressures $\geq$0.05 mbar can be explained by plume stopping, which occurs at a distance lower than the target to substrate spacing. In this pressure range, species arrive at the substrate surface by diffusion and simply condense on it without further diffusion along the surface. Furthermore, no damage is expected to be caused to the Sr buffer layer by the species from the plume for such high pressures. This was additionally confirmed by means of XPS studies. The samples prepared at pressures $\geq$0.05 mbar showed in the Si 2p region only elementary Si, indicated by a doublet Si $2p_{1/2}$ and Si $2p_{3/2}$. However, the samples prepared at 0.01 mbar or in a vacuum also contained a broad peak at higher binding energy, *i.e.*, a silicate phase (Fig. 2). This is formed due to interface mixing and reaction of high-energy species from the plasma plume with the Si substrate. Additional details of the experiment are presented in the ESI.† In summary, on the basis of XRR and XPS studies it is shown that the initial deposition of STO should be performed at pressures $\geq$0.05 mbar in order to ensure diffusion-like arrival of species to the substrate surface and consequently to avoid formation of the silicate at the interface. Furthermore, the pressure of 0.05 mbar seems to be the most suitable in terms of the layer density and deposition rate when compared to higher pressures.

Using the optimal pressure for the deposition, two additional experiments were performed. First the influence of temperature on the interface stability was studied. We showed that deposition at 260 °C already results in a thin silicate layer forming at the interface (brown curve). These results define also the optimal deposition temperature, which should be close to room temperature. In the second experiment, oxygen was used instead of argon. Deposition in oxygen would considerably simplify the whole synthesis process since no further consideration about oxidation would be necessary. However, also the oxygen atmosphere did not allow preparation of a clean STO/Si interface (pink curve), which is in accordance with the instability of the Sr buffer layer at such high oxygen pressure.

Optimization of the laser fluence

To assure the right composition of the initially deposited STO layer at room temperature and 0.05 mbar Ar pressure, a set of samples at several different fluences was prepared and analysed *ex situ* by XPS. Fig. S4a (ESI†) shows the variation of the Sr to Ti ratio with the laser fluence. A large excess of Sr compared to Ti can be noticed for all samples. As a reference, the composition of a commercial STO substrate (SurfaceNet, Germany) was measured in order to check the reliability of the method. The obtained value of N(Sr):N(Ti) = 1.13 indicates a slight overestimation of the Sr content compared to Ti, but still resembles the substrate actual composition. Since XPS is a surface sensitive technique the results may not reflect the composition of the whole STO layer. To verify this hypothesis, deep profiling by ion sputtering was performed on the sample

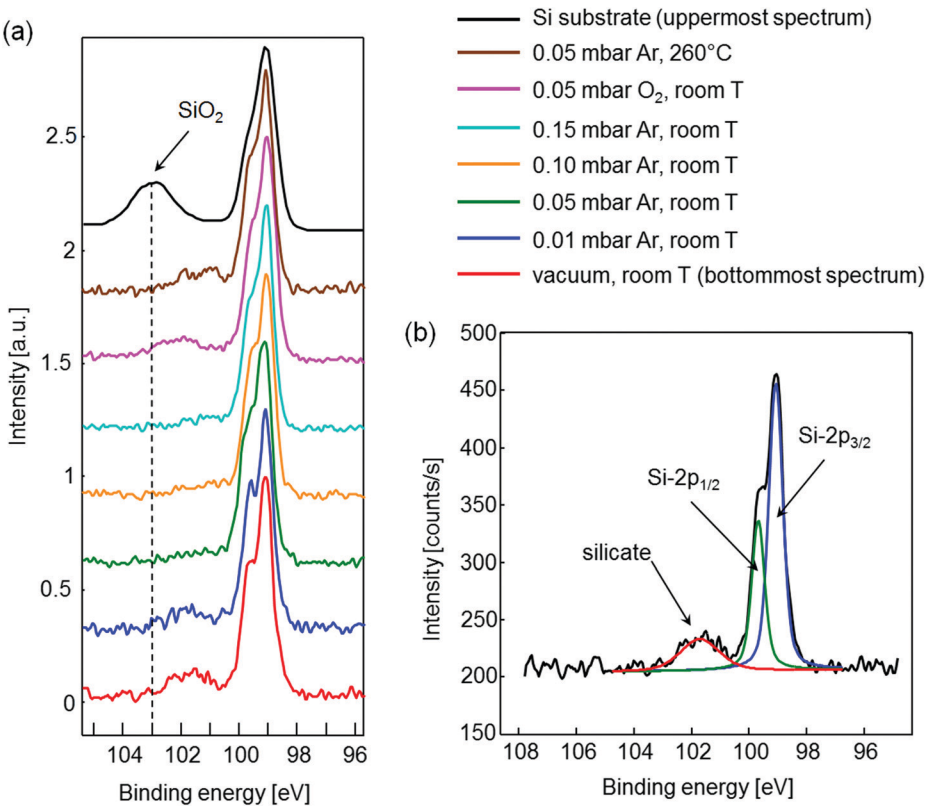

Fig. 2 (a) Si 2p XPS spectra from a 4.5 nm STO/Si sample prepared under experimental conditions, which differ in background gas (Ar and O_2), background gas pressure and substrate temperature (room *T* and 260 °C). (b) Si 2p XPS spectrum of the sample deposited in a vacuum. The Si 2p can be well fitted by the Si $2p_{1/2}$ and $2p_{3/2}$ core levels and by the silicate peak.

prepared at 1.5 J cm^{-2} in order to access the STO material at larger depths. From the depth profile in Fig. S4b (ESI†) it is evident that both the Sr and Ti atomic concentrations vary with sputtering time (sample depth), indicating an inhomogeneous distribution of the elements in the STO layer. Since the composition was calculated using a simplified model of a homogeneous matrix, this introduces an additional error in the concentration profile, which should therefore be viewed on a relative scale only. The largest difference between the concentrations of both elements can be observed in the surface region. With depth, the strontium concentration slightly decreases, while the Ti concentration increases. Such an inhomogeneity of Sr and Ti is not problematic if the overall content of Sr in the STO layer is equal to Ti due to complete homogenization of the layer during the crystallization step at higher temperature. Since the overall content of both metals cannot be derived from the XPS experiments Rutherford backscattering spectroscopy (RBS) was used for this purpose. The results of the analysis are presented in Fig. 3 and reveal that the overall composition of the STO layers is much closer to the ideal one compared to the surface composition. Regardless of the fluence used, all the samples still exhibit a larger atomic concentration of Sr compared to Ti. This can be explained by preferential scattering of the light plume species, *e.g.*, Ti in STO, during their flight towards the substrate. The plume species can undergo several collisions, both with the background gas molecules/atoms and among themselves.

In any scattering event, the lighter species diffuse to larger angles, resulting in a higher concentration of the heavier species (Sr for STO) along the direction normal to the substrate. In order to confirm the above described impact of the background gas on the stoichiometry, an additional set of samples was prepared in a vacuum where no scattering with the background gas is present. All the vacuum-deposited samples exhibit a stoichiometry very close to the ideal one (Fig. 3). The maximum difference between the Sr and Ti atomic concentration was encountered for a fluence of 1 J cm^{-2} (51.1% Sr and 48.9% Ti). Interpretation of the observed variation of the STO thin film stoichiometry with the laser fluence is rather difficult and it presumably results from an intricate combination between the plume–background gas interaction (*e.g.* preferential scattering) and the incongruent ablation of the STO target.[28,29] In the case of the vacuum-deposited samples also the impact of re-sputtering on the film stoichiometry should be taken into account due to the high kinetic energy of the plume species reaching the substrate.[30] Overall, we showed that a fluence of 1.5 J cm^{-2} results in the most stoichiometric STO layers (51.4% Sr and 48.6% Ti) for deposition performed at room temperature and 0.05 mbar Ar pressure. Nevertheless, Guillaume Saint-Girons and his co-workers recently demonstrated that an excess of Sr is indeed needed for formation of a single-crystal STO layer on Si by MBE at a moderate growth temperature from a partially separated amorphous mixture of SrO and TiO_2.[31] Additional Sr forms vertical SrO stacking faults and separate antiphase domains in the film. The excess of Sr in our most stoichiometric STO layers deposited at 0.05 mbar Ar pressure is close to the ideal value, determined in the above mentioned study, and is thus considered to have an advantageous effect on its crystallization.

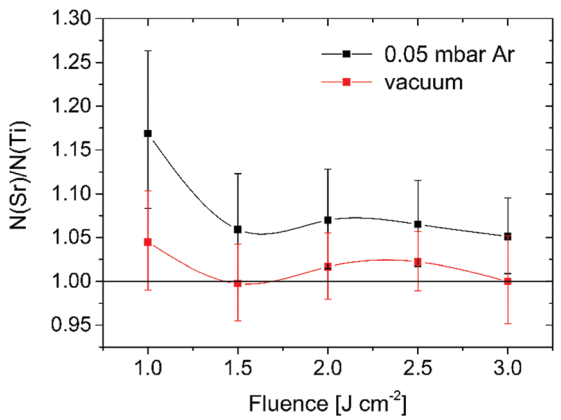

Fig. 3 Sr/Ti atomic ratio in STO films deposited at different fluences determined by RBS.

Oxidation of strontium and titanium

The most common way to deposit oxide films by PLD is to use an excess oxidant environment. The excess of oxygen helps to ensure that the grown film will be fully oxidized. However, in the case of STO deposition on Si the prepared Sr buffer layer cannot sustain an oxygen pressure higher than $\sim 1 \times 10^{-5}$ mbar. Introduction of an oxidant into the system is therefore one of the most important and delicate steps in the transition from silicon to STO. Since strontium (Sr) and titanium (Ti) have very different electronegativities, it is also expected that they have a different oxidation behavior. Sr becomes fully oxidized much more easily than Ti because of its smaller electronegativity.[32,33] As a result, the threshold for oxidation of titanium represents an important process parameter.[34] This threshold relates to the absolute minimum pressure where one can completely oxidize the metal and depends on the deposition temperature as well as the arrival rate of Ti. For a flux which corresponds to about one monolayer of Ti metal atoms per minute this pressure was experimentally found to be around 1.3–2.7 $\times$ 10^{-6} mbar.[35,36] In addition, it was shown that the presence of Sr promotes Ti oxidation by providing a different transition state that has a lower reaction barrier for Ti oxidation.[33] Consequently, the growth of STO can be conducted at even lower oxygen pressures than 1.3 $\times$ 10^{-6} mbar. Despite the resistivity of the buffer layer against oxidation at the pressures required for complete oxidation of Ti and Sr, we showed that at least a 0.05 mbar pressure is needed during the initial deposition of STO in order to completely avoid the reaction at the interface due to the collision of high-energy species from the plasma plume with the Si substrate. Such a high pressure allowed us to work in an inert atmosphere of Ar only. Regardless of the presence of oxygen in the STO target, we assumed that the deposition in Ar leads to oxygen deficient films, which could prevent STO from crystallizing in an epitaxial and highly crystalline manner. In order to determine the extent of Ti oxidation in STO films deposited at room temperature and 0.05 mbar Ar pressure, XPS depth profiling by ion sputtering

was performed. Fig. S5 (ESI†) shows a stack of Ti 2p XPS spectra obtained at different depths during XPS depth profiling. Two peaks, which correspond to the photoemission from the Ti $2p_{3/2}$ and Ti $2p_{1/2}$ energy levels, can be observed in all the spectra. The second feature in Fig. S5 (ESI†) is a shift of both peaks by 4.8 eV to lower binding energies in the XPS spectra obtained deeper in the sample (closer to the Si substrate). The Ti $2p_{3/2}$ binding energies of ~459.0 eV and 454.2 eV are characteristic for TiO_2 and metallic Ti, respectively. This indicates that in the upper part of the STO layer Ti is oxidized, while in the interior part it is metallic. The presence of TiO_2 can be explained by the exposure of the sample to air during transfer from the PLD to XPS UHV chamber, which was minimized to about 30 s. Another feasible reason for the presence of TiO_2 could be the oxidation caused by oxygen from the STO target. However, the presence of metallic Ti deeper in the sample is a clear indication of an oxygen deficient film and we believe it reflects the Ti oxidation state throughout the whole STO layer after PLD deposition in argon. Based on these results it can be concluded that the initial deposition of STO should be done in sections. We first need to grow amorphous STO with the right stoichiometry at room temperature and 0.05 mbar Ar pressure, preventing the formation of a silicate at the interface. Then we evacuate the argon and perform oxidation at an oxygen partial pressure sufficiently high to fully oxidize titanium as a second step. For complete oxidation of titanium across the whole thickness, the deposited STO layer from the first step should not be too thick. These two steps are then repeated until the optimal thickness for the crystallization at higher temperature is achieved.

Final deposition of STO

The final and most important goal was to grow an epitaxial STO layer on Si(001). Previous MBE studies revealed this step as most challenging and thus results from previous sections were combined and used in this final step; technical details are described in the ESI,† and schematically presented in Fig. S6 (ESI†). STO was grown on a Sr-passivated silicon substrate in a two-step procedure. In the first step the KCSD method was applied to deposit a 15 unit-cell thick STO seed layer. In this KCSD growth method, STO was deposited at low temperature and high Ar partial pressure to prevent oxidation of the buffer layer and implantation of the arriving species, respectively. The latter would damage the Sr-buffer layer and provoke interfacial reactions. Each ML of STO was then oxidized in a defined range of O_2 partial pressure, which assures oxidation of Ti and Sr, but not the underlying buffer. Crystallization of STO was performed for each 3 MLs of STO by annealing at elevated temperature under UHV. The thickness of the STO block and the crystallization temperature play a critical role in the crystallization process, as the layer critical thickness has to be reached, while maintaining the process thermal budget at a minimal level. In the second step of the procedure the rest of the STO layer is grown in a continuous way, at elevated temperature and relatively high O_2 partial pressure. The described growth protocol deviates from the one developed for MBE technology. Namely, it is adjusted for PLD growth, as the nature of these two processes and the nature of arriving particles are intrinsically different.

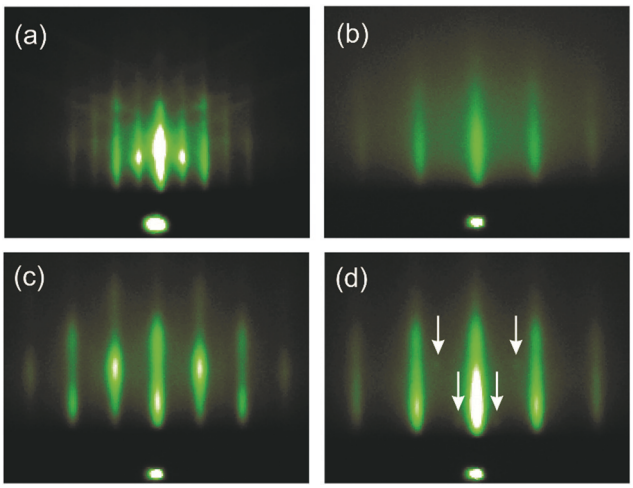

Fig. 4 RHEED patterns in the [110] azimuth of Sr-buffered Si taken (a) before the deposition of the STO seed layer and (b) after the second crystallization step of STO at 517 °C. RHEED patterns in the (c) [100] and (d) [110] azimuth after subsequent continuous deposition of STO at 517 °C. White arrows indicate additional spots, which arise from a small portion of crystallites with a deviating crystallographic orientation.

The results of the growth are presented in Fig. 4 and Fig. S7 (ESI†), which show RHEED patterns of STO after its deposition and crystallization. Deposition was initiated on a $(1 \times 2) + (2 \times 1)$ reconstructed surface, characteristic for the Sr-buffer layer (Fig. 4a and Fig. S7a, c, ESI†). After the deposition of 1 ML of STO at room temperature the intensity of integer and half-order streaks greatly decreased as a result of surface coverage with amorphous STO material, which does not exhibit any diffraction. Their faint appearance can be explained either by incomplete surface coverage or the penetration depth of the electron beam, which is somewhere in the range from 5 to 20 Å, depending on the material and incidence angle. After the deposition of 2 MLs the only visible feature is the central spot, while after 3 MLs only a high background can be observed (Fig. S7b and d, ESI†). Subsequently the 3 ML thick STO layer was heated to 517 °C for 15 min, which, however, does not result in the formation of any streaks in the RHEED pattern. During the crystallization of the next 3 ML thick amorphous STO layer, very weak streaks emerge after a few minutes and this is our first indication of epitaxial growth (Fig. 4b). The third deposition and subsequent crystallization further improve the intensity of the diffraction streaks. RHEED analysis in the [100] azimuth demonstrates comparable results. After the seed layer is formed additional STO is deposited on top of it, at elevated temperature. Subsequent deposition of 7366 pulses at 517 °C results in RHEED patterns with sharp and well defined streaks, as presented in Fig. 4c and d. Besides these, very weak spots lying on Laue circles are also present in the [110] direction, indicated by white arrows. These spots most likely arise from a small portion of crystallites with a deviating crystallographic orientation.

The XRD 2theta/theta scan of the sample shows that all the peaks present in the diffractogram can be described as Si or

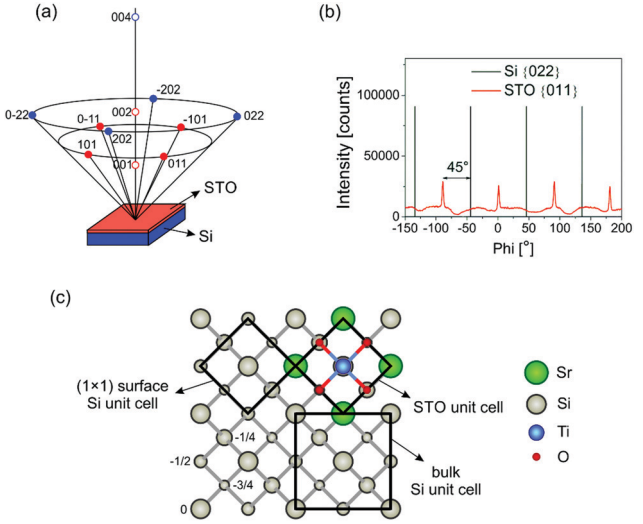

Fig. 5 (a) Family of asymmetric reciprocal lattice points for STO (filled red circles) and Si (filled blue circles), measured during the phi-scan. (b) X-ray diffraction measurements demonstrating the epitaxial relationship between STO and Si. The ϕ positions of the {011} and {022} peaks of the thin film and substrate, respectively, indicate the rotation of the STO unit cell by 45° with respect to the bulk Si cell. (c) Epitaxial matching of STO and Si(001). The numbers refer to the vertical position of the Si atoms with respect to the surface (set at zero), in units of the Si lattice constant.

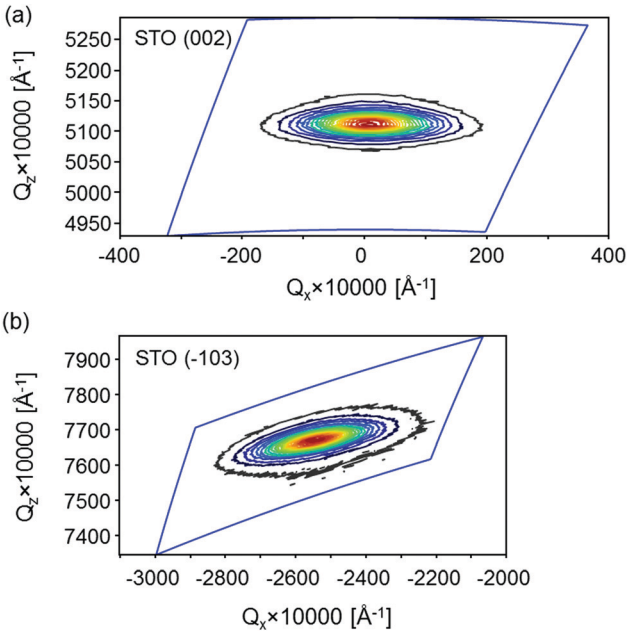

Fig. 6 STO reciprocal space maps around the (a) symmetric (002) reflection and (b) asymmetric (−103) reflection, plotted in reciprocal lattice units.

STO, indicating a single-phase film (Fig. S8, ESI†). In addition, only STO(00l) reflections are observed, showing the film out-of-plane relationship as STO(001)‖Si(001). In order to determine the epitaxial relation of the STO layer and the substrate, an azimuthal or phi (ϕ) scan was performed. The measurement was done on the {011} and {022} family of asymmetric crystallographic planes for STO and Si, respectively (Fig. 5a). The results of the ϕ scans are shown in Fig. 5b. The silicon substrate exhibits four peaks, which are 90° apart from each other, indicating its four-fold symmetry. Similarly, there are four peaks with the same spacing between them present in the ϕ scan of the STO layer, which reveal only one in-plane orientation of the film. These peaks are shifted over 45° relative to the substrate peaks, showing the in-plane epitaxial relationship of STO[110]‖Si[100], which is consistent with results in the literature where also epitaxial growth of STO on Si was achieved.[37,38] Thus, the STO unit cell is rotated 45° with respect to the conventional cubic cell of Si as shown in Fig. 5c. The reason for this STO in-plane rotation arises from the much better agreement of the STO unit cell parameter with the 1 × 1 surface Si cell compared to the conventional cell. The lattice constant of the 1 × 1 surface cell is 3.84 Å, which is very close to 3.905 Å of cubic STO and results in a 1.66% lattice mismatch only. Such an in-plane epitaxial relationship is evident also from the RHEED zone axis pattern (Fig. 4c and d). However, the presence of a few low intensity spots in the [110] direction implies that a small volume fraction of the STO layer does not obey this epitaxial relationship.

X-ray diffraction reciprocal space maps (RSMs) were recorded around the (002) and (−103) reflections in order to obtain the unit cell parameters and evaluate the mosaicity and lateral correlation of the STO layer (Fig. 6). Measurement of two reciprocal lattice spots (one symmetric and one asymmetric) instead of a single asymmetric one was performed due to the possible crystallographic tilt (offcut), which is common in epitaxial layers and represents the tilt of the layer lattice with respect to the surface (Fig. S9, ESI†). This tilt can arise when the substrate is offcut and when there are dislocations at the layer/substrate interface.[39] It was found that the in-plane ($a = b$) and out-of-plane (c) STO lattice parameters are 3.913 ± 0.006 Å and 3.911 ± 0.001 Å, respectively. These values differ slightly from those of the STO bulk single crystal (3.905 Å), which is due to the thermal expansion mismatch and STO nonstoichiometry, as discussed in detail in the ESI.†

The structural quality of the STO layer and its interface with silicon was examined closely using TEM. High-angle annular dark-field (HAADF) scanning-transmission electron microscopy (STEM) reveals the crystalline STO layer epitaxially grown on the Si substrate, seen as a bright region of the layer in Fig. 7a. However, regions of polycrystalline STO are also observed along the layer and can be differentiated from the epitaxial part by a strong contrast variation due to dynamic scattering, which is *e.g.* seen on the right-hand side of Fig. 7a. The presence of such additional orientations of the STO layer was already apparent from the RHEED analysis. Namely, in the [110] azimuth very weak spots are observed between the streaks (indicated by white arrows in Fig. 4d). These polycrystalline regions are not observed in the XRD 2theta/theta scan of the sample since their relative volume is below the detection limit. Fig. 7b shows a high resolution HAADF-STEM image of an epitaxial part of the layer and demonstrates its highly crystalline quality and nearly perfect epitaxial integration with the substrate. The crystal orientation of the STO layer in the out-of-plane and the in-plane directions confirms the XRD results, presented

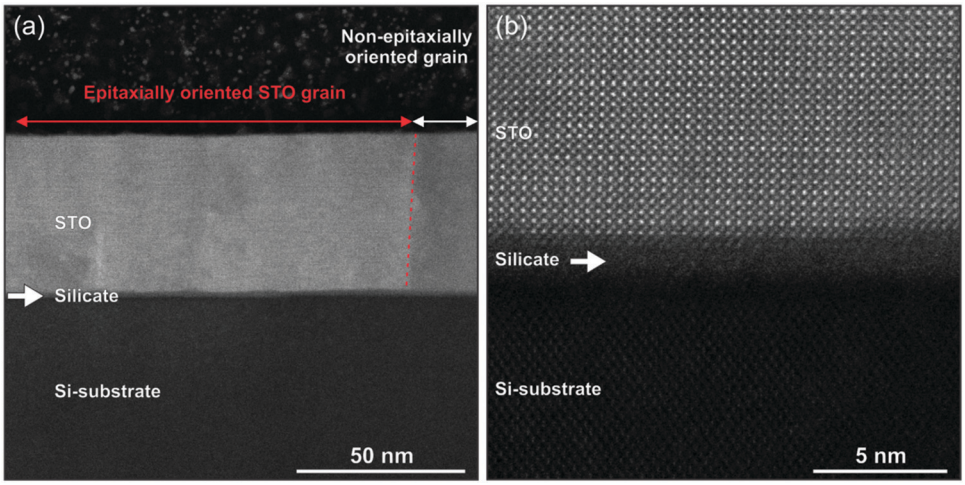

Fig. 7 (a) HAADF-STEM image oriented along the Si[110] substrate. The bright region shows crystalline STO epitaxially grown on the Si substrate. A non-epitaxially oriented STO grain is seen in the right-hand side of the image and can be identified by its contrast variation. (b) High-resolution HAADF-STEM image of a high-quality STO thin film and the presence of an amorphous silicate layer at the interface with Si. A near perfect epitaxial relation between Si (with visible [110] dumbbells) and STO (in [100] orientation) is revealed.

in Fig. S8 (ESI†) and Fig. 5b. In addition to the STO layer, which is 47 nm thick, TEM reveals that between STO and Si a tiny layer of an amorphous silicate with a thickness of about 2.5 nm is also present. The variation of the chemical composition across the interface was determined by atomically resolved electron energy-loss spectroscopy (EELS) maps, presented in Fig. S10 (ESI†). As discussed by Lei Zhang and his co-workers, such an interlayer can improve the thin film strain state. Namely, it relieves strain relaxation at the crystallization temperature, arising from lattice mismatch between STO and the Si substrate. However, upon cooling residual tensile strain is built in the thin film due to thermal expansion mismatch between the materials.[40]

The layers' electronic states were accessed by energy-loss near-edge structure (ELNES) and are presented in Fig. S11 (ESI†) for the (a) Si L_{23}, (b) Ti L_{23} and O K and (c) Si K and Sr L_{23} edges. In STO, the t_{2g} and e_g splitting of Ti L_{23}, as well as its O K spectral signatures, are characteristic of the STO perovskite cubic structure. In a Si substrate only the characteristic Si L_{23} peak at 99 eV is present. The different energy onset position and different spectral signatures of Si L_{23} and O K in the interface layer indicate the amorphous character of the layer. Furthermore, ELNES results also evidence a small amount of Ti and Sr signal in this layer. This confirms the formation of a strontium titanium silicate phase at the interface, instead of SiO_2, and can be attributed to the instability of direct contact between STO and Si. The thickness and composition of the interface layer were proven by XRR and XRS measurements as well. They are discussed in the ESI† (Fig. S12 and S13) and show that the formation of the silicate layer already starts during the crystallization steps of the STO seed, but is expected to become more intense during the subsequent continuous growth of STO at elevated temperature. In the film, bending contours were also observed in STEM. They are caused by Moiré's fringes between the crystal lattice and the scan grid and reveal the strain distribution across the film thickness. The presence of strain was already revealed by the XRD analysis, which showed that the STO unit cell parameters differ from that of the bulk single crystal, due to thermal expansion mismatch and STO nonstoichiometry.

The AFM image of the STO surface is shown in Fig. S14 (ESI†), demonstrating the smooth surface morphology with a measured RMS surface roughness of 2.7 Å.

Conclusions

This feasibility study demonstrated epitaxial growth of STO on a $(1 \times 2) + (2 \times 1)$ reconstructed Sr(1/2 ML)/Si(001) surface using PLD and showed its potential for implementation into oxide electronics. Detailed analysis of the initial deposition parameters proves to be extremely important, as the parameter window for successful growth is very narrow. With respect to MBE, the peculiarities of the PLD technology had to be considered in the growth protocol as well. The parameters for the deposition and oxidation periods play a crucial role in the quality of the STO layer and the interface and they have to be separated in time. For intermediate crystallization of the as-prepared layers a critical thickness has to be reached, while maintaining the process thermal budget at a minimal level, which enables us to kinetically trap the reaction between STO and Si and thus to minimize the thickness of the interface layer. These results present a milestone in silicon–oxide integration and open a new technological route for oxide electronics, which demonstrate rich functionalities beyond the state-of-the-art silicon platform.

Funding

The research was financially supported by the Slovenian Research Agency (Project No. P2-0091, J2-9237) and Ministry of Education, Science and Sport of the Republic of Slovenia

(SIOX projects). This work was also funded by the European Union Council under the 7th Framework Program grant no. NMP3-LA-2010-246102 IFOX. J. V. and G. V. T. acknowledge funding from the Fund for Scientific Research Flanders under project no. G.0044.13N.

Conflicts of interest

There are no conflicts to declare.

References

1 S. R. Bakaul, C. R. Serrao, M. Lee, C. W. Yeung, A. Sarker, S.-L. Hsu, A. K. Yadav, L. Dedon, L. You, A. I. Khan, J. D. Clarkson, C. Hu, R. Ramesh and S. Salahuddin, Single crystal functional oxides on silicon, *Nat. Commun.*, 2016, **7**, 10547.

2 M. P. Warusawithana, C. Cen, C. R. Sleasman, J. C. Woicik, Y. L. Li, L. F. Kourkoutis, J. A. Klug, H. Li, P. Ryan, L. P. Wang, M. Bedzyk, D. A. Muller, L. Q. Chen, J. Levy and D. G. Schlom, A ferroelectric oxide made directly on silicon, *Science*, 2009, **324**, 367–370.

3 J. W. Park, D. F. Bogorin, C. Cen, D. A. Felker, Y. Zhang, C. T. Nelson, C. W. Bark, C. M. Folkman, X. Q. Pan, M. S. Rzchowski, J. Levy and C. B. Eom, Creation of a two-dimensional electron gas at an oxide interface on silicon, *Nat. Commun.*, 2010, **1**, 6.

4 S. H. Baek, J. Park, D. M. Kim, V. A. Aksyuk, R. R. Das, S. D. Bu, D. A. Felker, J. Lettieri, V. Vaithyanathan, S. S. N. Bharadwaja, N. Bassiri-Gharb, Y. B. Chen, H. P. Sun, C. M. Folkman, H. W. Jang, D. J. Kreft, S. K. Streiffer, R. Ramesh, X. Q. Pan, S. Trolier-McKinstry, D. G. Schlom, M. S. Rzchowski, R. H. Blick and C. B. Eom, Giant Piezoelectricity on Si for Hyperactive MEMS, *Science*, 2011, **334**, 958–961.

5 A. A. Demkov and A. B. Posadas, *Integration of Functional Oxides with Semiconductors*, 2014.

6 S. H. Baek and C. B. Eom, Epitaxial integration of perovskite-based multifunctional oxides on silicon, *Acta Mater.*, 2013, **61**, 2734–2750.

7 D. W. Oh, J. Ravichandran, C. W. Liang, W. Siemons, B. Jalan, C. M. Brooks, M. Huijben, D. G. Schlom, S. Stemmer, L. W. Martin, A. Majumdar, R. Ramesh and D. G. Cahill, Thermal conductivity as a metric for the crystalline quality of $SrTiO_3$ epitaxial layers, *Appl. Phys. Lett.*, 2011, **98**, 3.

8 X. M. Hu, H. Li, Y. Liang, Y. Wei, Z. Yu, D. Marshall, J. Edwards, R. Droopad, X. Zhang, A. A. Demkov, K. Moore and J. Kulik, The interface of epitaxial $SrTiO_3$ on silicon: in situ and ex situ studies, *Appl. Phys. Lett.*, 2003, **82**, 203–205.

9 G. Niu, G. Saint-Girons, B. Vilquin, G. Delhaye, J. L. Maurice, C. Botella, Y. Robach and G. Hollinger, Molecular beam epitaxy of $SrTiO_3$ on Si(001): early stages of the growth and strain relaxation, *Appl. Phys. Lett.*, 2009, **95**, 3.

10 G. Niu, W. W. Peng, G. Saint-Girons, J. Penuelas, P. Roy, J. B. Brubach, J. L. Maurice, G. Hollinger and B. Vilquin, Direct epitaxial growth of $SrTiO_3$ on Si(001): interface, crystallization and IR evidence of phase transition, *Thin Solid Films*, 2011, **519**, 5722–5725.

11 G. Niu, J. Penuelas, L. Largeau, B. Vilquin, J. L. Maurice, C. Botella, G. Hollinger and G. Saint-Girons, Evidence for the formation of two phases during the growth of $SrTiO_3$ on silicon, *Phys. Rev. B: Condens. Matter Mater. Phys.*, 2011, **83**, 9.

12 H. Li, X. Hu, Y. Wei, Z. Yu, X. Zhang, R. Droopad, A. A. Demkov, J. Edwards, K. Moore, W. Ooms, J. Kulik and P. Fejes, Two-dimensional growth of high-quality strontium titanate thin films on Si, *J. Appl. Phys.*, 2003, **93**, 4521–4525.

13 J. C. Woicik, H. Li, P. Zschack, E. Karapetrova, P. Ryan, C. R. Ashman and C. S. Hellberg, Anomalous lattice expansion of coherently strained $SrTiO_3$ thin films grown on Si(001) by kinetically controlled sequential deposition, *Phys. Rev. B: Condens. Matter Mater. Phys.*, 2006, **73**, 5.

14 X. Gu, D. Lubyshev, J. Batzel, J. M. Fastenau, W. K. Liu, R. Pelzel, J. F. Magana, Q. Ma, L. P. Wang, P. Zhang and V. R. Rao, Commercial molecular beam epitaxy production of high quality $SrTiO_3$ on large diameter Si substrates, *J. Vac. Sci. Technol., B*, 2009, **27**, 1195–1199.

15 D. M. Schaadt, E. T. Yu, V. Vaithyanathan and D. G. Schlom, Nanoscale current transport in epitaxial $SrTiO_3$ on $n(+)$-Si investigated with conductive atomic force microscopy, *J. Vac. Sci. Technol., B*, 2004, **22**, 2030–2034.

16 J. Q. He, C. L. Jia, V. Vaithyanathan, D. G. Schlom, J. Schubert, A. Gerber, H. H. Kolhstedt and R. H. Wang, Interfacial reaction in the growth of epitaxial $SrTiO_3$ thin films on (001) Si substrates, *J. Appl. Phys.*, 2005, **97**, 6.

17 L. V. Goncharova, D. G. Starodub, E. Garfunkel, T. Gustafsson, V. Vaithyanathan, J. Lettieri and D. G. Schlom, Interface structure and thermal stability of epitaxial $SrTiO_3$ thin films on Si(001), *J. Appl. Phys.*, 2006, **100**, 6.

18 L. F. Kourkoutis, C. S. Hellberg, V. Vaithyanathan, H. Li, M. K. Parker, K. E. Andersen, D. G. Schlom and D. A. Muller, Imaging the phase separation in atomically thin buried $SrTiO_3$ layers by electron channeling, *Phys. Rev. Lett.*, 2008, **100**, 4.

19 S. B. Mi, C. L. Jia, V. Vaithyanathan, L. Houben, J. Schubert, D. G. Schlom and K. Urban, Atomic structure of the interface between $SrTiO_3$ thin films and Si(001) substrates, *Appl. Phys. Lett.*, 2008, **93**, 3.

20 R. D. Vispute, J. Narayan, K. Dovidenko, K. Jagannadham, N. Parikh, A. Suvkhanov and J. D. Budai, Heteroepitaxial structures of $SrTiO_3$/TiN on Si(100) by in situ pulsed laser deposition, *J. Appl. Phys.*, 1996, **80**, 6720–6724.

21 S. J. Wang and C. K. Ong, Epitaxial Y-stabilized ZrO_2 films on silicon: dynamic growth process and interface structure, *Appl. Phys. Lett.*, 2002, **80**, 2541–2543.

22 M. Kondo, K. Maruyama and K. Kurihara, Epitaxial ferroelectric thin films on silicon substrates for future electronic devices, *Fujitsu Sci. Tech. J.*, 2002, **38**, 46–53.

23 F. Sanchez, R. Aguiar, V. Trtik, C. Guerrero, C. Ferrater and M. Varela, Epitaxial growth of $SrTiO_3$ (00*h*), (0*hh*), and (*hhh*) thin films on buffered Si(001), *J. Mater. Res.*, 1998, **13**, 1422–1425.

24 D. Klement, M. Spreitzer and D. Suvorov, Formation of a strontium buffer layer on Si(001) by pulsed-laser deposition through the Sr/Si(001)(2 × 3) surface reconstruction, *Appl. Phys. Lett.*, 2015, **106**, 071602.
25 M. Spreitzer, R. Egoavil, J. Verbeeck, D. H. A. Blank and G. Rijnders, Pulsed laser deposition of $SrTiO_3$ on a H-terminated Si substrate, *J. Mater. Chem. C*, 2013, **1**, 5216–5222.
26 Z. Jovanović, M. Spreitzer, J. Kovač, D. Klement and D. Suvorov, Silicon surface deoxidation using strontium oxide deposited with the pulsed laser deposition technique, *ACS Appl. Mater. Interfaces*, 2014, **6**, 18205–18214.
27 Z. Jovanovic, M. Spreitzer, U. Gabor and D. Suvorov, Control of SrO buffer-layer formation on Si(001) using the pulsed-laser deposition technique, *RSC Adv.*, 2016, **6**, 82150–82156.
28 T. E. Itina, W. Marine and M. Autric, Monte Carlo simulation of pulsed laser ablation from two-component target into diluted ambient gas, *J. Appl. Phys.*, 1997, **82**, 3536–3542.
29 S. Wicklein, A. Sambri, S. Amoruso, X. Wang, R. Bruzzese, A. Koehl and R. Dittmann, Pulsed laser ablation of complex oxides: the role of congruent ablation and preferential scattering for the film stoichiometry, *Appl. Phys. Lett.*, 2012, **101**, 5.
30 J. Schou, Physical aspects of the pulsed laser deposition technique: the stoichiometric transfer of material from target to film, *Appl. Surf. Sci.*, 2009, **255**, 5191–5198.
31 G. Saint-Girons, R. Bachelet, R. Moalla, B. Meunier, L. Louahadj, B. Canut, A. Carretero-Genevrier, J. Gazquez, P. Regreny, C. Botella, J. Penuelas, M. G. Silly, F. Sirotti and G. Grenet, Epitaxy of SrTiO3 on Silicon: The Knitting Machine Strategy, *Chem. Mater.*, 2016, **28**, 5347–5355.
32 J. Lettieri, J. H. Haeni and D. G. Schlom, Critical issues in the heteroepitaxial growth of alkaline-earth oxides on silicon, *J. Vac. Sci. Technol., A*, 2002, **20**, 1332–1340.
33 Y. Liang, Y. Wei, X. M. Hu, Z. Yu, R. Droopad, H. Li and K. Moore, Heteroepitaxy of $SrTiO_3$ on vicinal Si(001): growth and kinetic effects, *J. Appl. Phys.*, 2004, **96**, 3413–3416.
34 K. Orsel, R. Groenen, B. Bastiaens, G. Koster, G. Rijnders and K.-J. Boller, Influence of the oxidation state of SrTiO3 plasmas for stoichiometric growth of pulsed laser deposition films identified by laser induced fluorescence, *APL Mater.*, 2015, **3**, 106103.
35 J. Heyd, G. E. Scuseria and M. Ernzerhof, Hybrid functionals based on a screened Coulomb potential, *J. Chem. Phys.*, 2006, **124**, 1.
36 A. A. Demkov and A. B. Posadas, *Integration of Functional Oxides with Semiconductors*, 2014.
37 Y. Wang, C. Ganpule, B. T. Liu, H. Li, K. Mori, B. Hill, M. Wuttig, R. Ramesh, J. Finder, Z. Yu, R. Droopad and K. Eisenbeiser, Epitaxial ferroelectric $Pb(Zr,Ti)O_3$ thin films on Si using $SrTiO_3$ template layers, *Appl. Phys. Lett.*, 2002, **80**, 97–99.
38 G. Y. Yang, J. M. Finder, J. Wang, Z. L. Wang, Z. Yu, J. Ramdani, R. Droopad, K. W. Eisenbeiser and R. Ramesh, Study of microstructure in $SrTiO_3$/Si by high-resolution transmission electron microscopy, *J. Mater. Res.*, 2002, **17**, 204–213.
39 M. A. Moram and M. E. Vickers, X-ray difraction of III-nitrides, *Rep. Prog. Phys.*, 2009, **72**, 036502.
40 L. Zhang, Y. Yuan, J. Lapano, M. Brahlek, S. Lei, B. Kabius, V. Gopalan and R. Engel-Herbert, Continuously Tuning Epitaxial Strains by Thermal Mismatch, *ACS Nano*, 2018, **12**, 1306–1312.